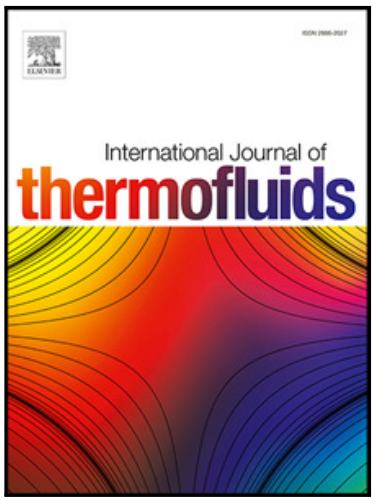


# Investigation of Natural Convection and Entropy Generation in a Porous Titled Z-Staggered Cavity Saturated by TiO2-Water Nanouid

Qusay Rasheed Al-Amir , Hameed K. Hamzah , Farooq H. Ali , M. Hatami , Wael Al-Kouz , Ahmed Al-Manea , Raed Al-Rbaihat , Ali Alahmer

PII: S2666-2027(23)00112-X
DOI: https://doi.org/10.1016/j.ijft.2023.100395
Reference: IJTF 100395

To appear in: *International Journal of Thermofluids*

Received date: 4 January 2023
Revised date: 8 June 2023
Accepted date: 9 June 2023

Please cite this article as: Qusay Rasheed Al-Amir , Hameed K. Hamzah , Farooq H. Ali , M. Hatami , Wael Al-Kouz , Ahmed Al-Manea , Raed Al-Rbaihat , Ali Alahmer , Investigation of Natural Convection and Entropy Generation in a Porous Titled Z-Staggered Cavity Saturated by TiO2-Water Nanouid, *International Journal of Thermofluids* (2023), doi: https://doi.org/10.1016/j.ijft.2023.100395

# Investigation of Natural Convection and Entropy Generation in a Porous Titled Z-Staggered Cavity Saturated by $TiO_2$-Water Nanofluid

Qusay Rasheed Al-Amir[1], Hameed K. Hamzah[1], Farooq H. Ali[1], M. Hatami[2], Wael Al-Kouz[3,4], Ahmed Al-Manea[5], Raed Al-Rbaihat[6], Ali Alahmer[6,7,*]

[1] Mechanical Engineering Department, College of Engineering, Babylon University, Babylon, Iraq
Babylon, Iraq
[2] Ferdowsi University of Mashhad, Department of Mechanical Engineering, Mashhad, Iran
[3] College of Engineering and Technology, American University of the Middle East, Kuwait
[4] Department of Mechanical and Maintenance Engineering, School of Applied Technical Sciences, German
Jordanian University, Amman 11180, Jordan
[5]Al-Furat Al-Awsat Technical University, Iraq
[6] Department of Mechanical Engineering, College of Engineering, Tafila Technical University, Tafila 66110, Jordan
[7] Department of Industrial and Systems Engineering, Auburn University, Auburn, AL 36849

***Corresponding author:** aza0300@auburn.edu or a.alahmer@ttu.edu.jo (Ali Alahmer)

## Highlights

- The entropy generation and natural convection in a Z-staggered cavity filled with a porous media filled with a $TiO_2$-water nanofluid were investigated.
- The fundamental equations are solved using the Galerkin Finite Element Method (GFEM), and the results are described in detail.
- This study is essential for a variety of applications, including heat exchanger cooling of electronic equipment, solar pond, natural gas tank storage, material, and gas transference.
- Increasing the volume fraction of nanoparticles enhanced the heat transfer but reduced the maximum values of streamlines owing to the more significant density of nanofluid.
- The inclination angle considerably influenced natural convection; the most significant value of streamline occurred at an inclination angle ($\gamma$) of 60.

**Abstract**

The natural convection within enclosures along with entropy generation minimization plays a crucial role in various applications, particularly when they involve the utilization of nanofluids and porous media. This phenomenon plays a crucial role in enhancing heat transfer, fluid flow, and overall system performance. By understanding and optimizing the natural convection and entropy generation processes, it becomes possible to improve the efficiency and effectiveness of various thermal management systems, such as heat exchangers, electronic cooling systems, and renewable energy devices. Moreover, the integration of nanofluids and porous media introduces additional complexities and opportunities for enhancing heat transfer and fluid flow characteristics within enclosures. The current study investigates entropy generation (Sgen) and natural convection in a Z-staggered cavity filled with a porous media filled with a $TiO_2$-water nanofluid. The symmetrical enclosures with dimensions of 0.6 L × 0.5 L are considered, and the media contain a porous material saturated with $TiO_2$-water nanofluid. The wavy left and right vertical walls of the staggered enclosure were maintained hot and cold at temperatures ($T_h$) and ($T_c$), respectively. All the straight horizontal walls were considered insulated and impermeable. The fundamental equations are solved using the Galerkin Finite Element Method (GFEM), and the results are described in detail. The key result was that raising the Rayleigh number (Ra) and nanoparticle volume fraction increased heat transmission. Specifically, increasing the Rayleigh number from ($Ra=10^5$) to ($Ra=10^6$) leads in an 80% increase in heat transfer. However, as the density of the nanofluid increases, the highest values of streamlines decrease. Decreasing the Darcy number (Da) educed the maximum values of the streamlines and average Nusselt number (Nu). Additionally, increasing the heat generation factor ($\lambda$) from ($\lambda=0$) to ($\lambda=5$) decreases the Nusselt number by 30%. Furthermore, the most effective streamline value was achieved at an inclination angle ($\gamma$) of 60.

**Keywords:** Natural convection; porous medium; nanofluid; staggered enclosure; corrugated wall

## 1. Introduction

Natural convection (N.C.) inside enclosures has attracted a significant amount of interest due to its many practical applications. Solar collectors are one of these applications [1]. Based on the studies and review articles, there are various enclosure shapes, such as square and rectangular enclosures, with the highest number of publications [2,3]. Other enclosure shapes include triangular, rhombus, parallelogrammic, trapezoidal, and wavy. Recently, new shapes of more sophisticated enclosures have developed, known as combined enclosures, which they are formed by merging two simple enclosure shapes. This brings the combined enclosure shape closer to reality. In addition, incorporating nanoparticles into the porous media (P.M.) is a potential strategy for improving heat transfer (H.T.) [4–7]. Most previous studies have focused on simple shapes. Turan et al. [8] proposed a square enclosure and used FLUENT to examine the non-Newtonian fluid flow within the square enclosure. The influence of the tilt angle of the square enclosure was demonstrated in [9]. However, the square enclosure filled with nanofluid was examined by Ho et al. [10]. The study revealed that introducing nanoparticles boosted the thermal rate of H.T. substantially. Kang et al. [11] investigated the effect of internal circular body positions in a square enclosure. Al-Zamily [12] investigated N.C. in a square enclosure filled with a nanofluid and porous medium across a broad range of Ra and Da numbers, nanofluid loading, and porous layer thickness. Al-Amir et al. [13] examined the effect of the Prandtl number (Pr) on N.C. filled by a nanoporous layer on the left layer with non-Newtonian fluid in the right layer separated by a wavy wall. The N.C. in different shapes, such as rectangular [14–17][18], triangular [19,20], square [21], trapezoidal [22,23], parallelogrammic [24,25], and rhombus [26], has been studied in the same manner as the square enclosure. Dutta et al. [27] analyzed the heat exchange and entropy production caused by magnetohydrodynamic (MHD)- N.C. in rhombic enclosures containing Cu-water nanofluids. According to their findings, the Sgen rate decreases as Ha increases for wide range of Ra and enclosure tilt angles. A computational analysis of Sgen for a rhombic enclosure with a 30° inclination angle and a porous material was provided in [28]. For any value of the Ra and Da

values, the most minor and maximum entropy generation (Sgen) was achieved for phase shift angles π/4 and 3π/4, respectively. Dutta et al. [29] examined the thermal energy transport mediated by MHD buoyancy within a quadrantal enclosure filled with nanofluid. Their findings demonstrated that reducing the enclosure's sector angle enhanced heat transmission rate and vice versa. In this approach, a geometrical variation has the same effect on how the Qrate is altered as Ra, ϕ, and Ha. Dutta et al. [30] evaluated the irreversibility properties in a quadrantal porous cavity heated uniformly from the bottom wall. It demonstrated that fluid friction irreversibility dominates at higher values of Ra (=$10^6$) and Da (=$10^{-2}$). Many review papers detailed earlier efforts considering many factors, such as the effect of various dimensionless numbers, inclination angle, nanofluid loading, aspect ratio, Sgen, MHD, and the inner body are available in [31–37] .

It has also been shown that the corrugated technique improves H.T., which has piqued the interest of various researchers. Using a finite volume approach, Oztop et al. [38] investigated the effect of heat production within a wavy enclosure. The influence of different wavy patterns along with nanofluid and the Sgen has been studied by Esmaeilpour and Abdollahzadeh [39]. Furthermore, a comparison study of the influence of several nanofluid-filled complex wavy enclosures was conducted by Cho et al. [40]. Their results were crucial as they stated that the wavy surface affects Sgen. They also found Cu-water was the best choice compared to other nanofluids. Hanif et al. [41] used a vertical cone in a P.M. to evaluate the heat and flow transfer rates in a hybrid nanofluid containing a suspension of hybrid nanoparticles (Cu-$Fe_3O_4$). Manaa et al. [42] tested thermo-solutal N.C. in a cubical enclosure that was differentially heated and contained a micropolar CNT/water nanofluid. Bhardwaj et al. [43] evaluated N.C. in a triangular enclosure with a corrugated (wavy) wall on its left using finite difference formulation. They demonstrated that the inclusion of a wavy wall generates more Sgen owing to increased fluid friction than that of a flat surface. However, the wavy wall also improves H.T. compared to the flat surface. Hussain [44] investigated the double-diffusive MHD free convection in an inclined wavy enclosure. Bhardwaj and Dalal [45] used the finite element method (FEM) to study the Sgen in a triangular with a wavy

corrugated wall filled by a porous medium. Sharma [46] proposed using FEM to examine steady-state H.T. and predict the thermal conductivity of composite materials. They used a variety of meshing methods to mesh these intricately constructed composites. The mesh quality was assessed using the mesh metrics of element quality and skewness before conducting a convergence study in order to ensure mesh-independent results. Muthukumar [47] examined the impact of uniform and non-uniform bottom wall heating on mixed convective heat transmission in a square porous chamber filled with nanofluid and surrounded by a magnetic field. It has been shown that increasing the solid volume percentage increases the Qrate regardless of the magnetic field. Meshram [48] examined the effect of tilt angle affected N.C. features and entropy production in a two-dimensional square enclosure saturated with a porous medium. Their results indicated that the variation in entropy production rate with an inclination angle is considerable for larger values of the Darcy number. Hatami [49] addressed N.C. between internal cylinders in a wavy enclosure using the response surface approach to figure out the optimal wavy profile. They also identified a crucial value for the inner cylinder diameter at which buoyancy-driven H.T. reduces. Abdulkadhim et al. [50] used a finite element method to calculate the magnetic field while considering internal heat generation and absorption inside a nanofluid-filled wavy enclosure with an inner circular body. Mokaddes et al.[51] studied the N.C. with inner heat-generating circular bodies in a hybrid nanofluid wavy enclosure using finite element formulation. Aboud et al. [52] employed a FEM to investigate N.C. inside a wavy enclosure with various inner body shapes, such as (circular, triangular, square, and rhombus). There is a lot of interest in this field of N.C. within the combined enclosure, such as I-shaped enclosures [53–56], U-shaped enclosures [57,58], and T-shaped enclosures [59–61]. Islam et al. [62] minvestigated numerical research about natural porous convection in a square cavity with partially corrugated vertical walls. The porous cavity was filled with $Al_2O_3$ nanoparticles with water. However, the study has critical limitations regarding H.T. within a staggered enclosure [63].

The significance of natural convection within enclosures extends beyond standalone applications and finds relevance in various fields. For instance, in the realm of heat exchanger cooling for electronic equipment, natural convection plays a vital role in dissipating excess heat generated during operation, ensuring optimal performance and preventing damage. Solar pond systems utilize natural convection to create thermal stratification, maximizing the efficiency of energy collection. In the context of natural gas tank storage, understanding natural convection is crucial for maintaining temperature uniformity and preventing stratification, which can impact the quality and stability of stored gas. Moreover, in material processing applications, such as casting and solidification, controlling natural convection is essential for achieving desired material properties and minimizing defects. Similarly, natural convection is of utmost importance in processes involving gas transfer, such as ventilation systems and chemical reactors, where efficient heat and mass transfer are critical for overall system performance.

While the complexities of staggered shapes within enclosures have been explored in a few studies, the specific impact of corrugated walls, boundary conditions, and their interplay with entropy generation, heat transfer, and fluid structures is investigated in our research. Insights into how natural convection patterns and entropy generation are influenced by geometric variations are gained by examining the effects of corrugated walls. Additionally, the unique configuration of a staggered enclosure with corrugated walls, boundary conditions, and exposure to a porous medium saturated with nanofluid is investigated in our study. This combination of factors results in additional complexities being introduced to the problem, making it a compelling area for investigation.

To the best of our knowledge, no prior studies have specifically examined the effects of corrugated (wavy) walls on natural convection and entropy generation within a staggered enclosure, particularly from the left side walls. By addressing this research gap, our study contributes to the existing literature by shedding light on the distinct challenges and phenomena associated with such configurations. Our findings provide valuable insights into the interplay between wall geometry,

boundary conditions, and fluid dynamics, facilitating a deeper understanding of the natural convection process within enclosures.

The importance of our research is emphasized in the concluding part of the introduction, where we highlight the diverse range of applications that can benefit from a deeper understanding of natural convection inside enclosures. Improved knowledge in this area has practical implications for enhancing heat exchanger efficiency, optimizing solar energy systems, ensuring stable gas storage, and enhancing various industrial processes involving fluid dynamics and heat transfer. By providing valuable insights and addressing the specific complexities of the investigated configuration, our study contributes to the advancement of these applications, enabling more efficient and effective thermal management and system design.

## 2. Definition of a Physical Problem

The physical issue with the coordinate system under the study is described in Fig. 1. It contains of a staggering enclosure with an overlapping of the corners (right-top corner of the lower enclosure and left-bottom corner of the upper enclosure). The symmetrical enclosures with dimensions of 0.6 L × 0.5 L contain a P.M. saturated with $TiO_2$-water nanofluid (Table 1). The enclosure is maintained at temperatures ($T_h$) and ($T_c$) on the left and right wavy vertical walls, respectively. All straight horizontal walls are adiabatic and impermeable. A sinusoidal curve profile can follow the wavy vertical walls function and governing equations [64].

$$x = A\sin(\pi n y) \tag{1}$$

Where $A$ is oscillation amplitude, and n is number of waves.

The following assumptions underlay this study:

1- Flow is two-dimensional, laminar, newtonian, and incompressible.

2- The radiation heat exchange, Forchheimer's inertia, and Joule heating are neglected [65].

3- All thermophysical parameters are constant, except the variations in density, which introduce a body force element into the momentum equation's vertical component.

4- The porous medium's solid matrix and the nanofluid filling the pores are in thermal equilibrium.

5- This study considers heat generation from viscous dissipation and Darcy dissipation.

6- Gravitational force is exerted vertically downward.

7- The Boussinesq approximations are undertaken to be valid.

The thermophysical characteristics of the Titanium Oxide nanoparticle and water are listed in Table 1. Different dimensionless parameters can be used to describe the present situation, such as the Rayleigh number (Ra = $10^3$, $10^4$, $10^5$, and $10^6$), the Darcy number ($Da$ = $10^{-1}$, $10^{-2}$, $10^{-3}$, $10^{-4}$, and $10^{-5}$), the oscillation amplitude ($A$ = 0.02, 0.04, 0.06, 0.08, and 0.1 L), Volume fraction ($\emptyset = 0$, 0.02, 0.04 and 0.06), and the inclination angle varied as ($\gamma$ = 0°, 30°, 45°, 60° and 90°). The non-dimensional Heat generation factor ($\lambda$) ranged from 0 to 20.

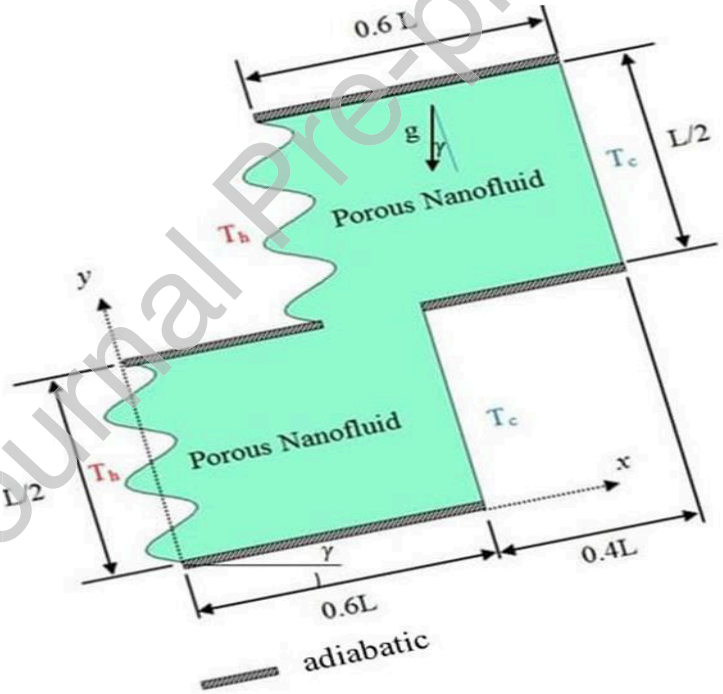


**Fig. 1** Simplified diagram of physical of the present study

**Table 1** Properties of base fluids and nanoparticles (A. Al-Zamily [12])

| Material/Properties | ρ (kg/m$^3$) | $C_p$ (J/kg.K) | k (W/m.K) | β (1/K) |
|---|---|---|---|---|
| Water | 997.1 | 4179 | 0.613 | 21*10$^{-5}$ |
| Titanium Oxide | 4250 | 686.2 | 8.9538 | 0.9*10$^{-5}$ |

## 3. Governing Equation and Boundary Conditions

According to the previous assumptions and physical definition, the following equations can be described our situation as follows [12]:

$$\frac{\partial u^*}{\partial x}+\frac{\partial v^*}{\partial y}=0 \tag{2}$$

$$u^*\frac{\partial u^*}{\partial x}+v^*\frac{\partial u^*}{\partial y}=-\varepsilon^2\frac{1}{\rho_{nf}}\frac{\partial p}{\partial x}+\varepsilon\frac{1}{\nu_{nf}}\left(\frac{\partial^2 u^*}{\partial x^2}+\frac{\partial^2 u^*}{\partial y^2}\right)-\varepsilon^2.\frac{1}{\nu_{nf}}.\frac{u^*}{K}+\ \varepsilon^2\beta_{nf}g(T-T_c)sin\gamma \tag{3}$$

$$u^*\frac{\partial v^*}{\partial x}+v^*\frac{\partial v^*}{\partial y}=-\varepsilon^2\frac{1}{\rho_{nf}}\frac{\partial p}{\partial y}+\varepsilon\frac{1}{\nu_{nf}}\left(\frac{\partial^2 v^*}{\partial x^2}+\frac{\partial^2 v^*}{\partial y^2}\right)-\varepsilon^2.\frac{1}{\nu_{nf}}.\frac{v^*}{K}+\varepsilon^2\beta_{nf}\ \ g\ (T-T_c\ )cos\ \gamma \tag{4}$$

$$u^*\frac{\partial T}{\partial x}+v^*\frac{\partial T}{\partial y}=\frac{\alpha_{eff}}{\alpha_f}\left(\frac{\partial^2 T}{\partial x^2}+\frac{\partial^2 T}{\partial y^2}\right)+Q_\circ(T-T_c) \tag{5}$$

The corresponding boundary conditions in dimension manner are listed as:

$u^*=0\ ;\ v^*=0\ ;\quad \mathrm{T}=\mathrm{T_h}$ at the hot left walls of the enclosure (6)

$u^*=0\ ;\ v^*=0\ ;\quad \mathrm{T}=\mathrm{T_c}$ at the cold right walls of the enclosure (7)

$u^*=0\ ;\quad v^*=0\ ;\quad \frac{\partial T}{\partial Y}=0$, at the insulated walls (8)

The form of dimensionless following equations of the situation are presented below :

$$\frac{\partial U^*}{\partial X}+\frac{\partial V^*}{\partial Y}=0 \tag{9}$$

$$U^*\frac{\partial U^*}{\partial X}+V^*\frac{\partial U^*}{\partial Y}=-\varepsilon^2\frac{\partial P}{\partial X}+\varepsilon.\frac{1}{\nu_{nf}\alpha_f}.\left(\frac{\partial^2 U^*}{\partial X^2}+\frac{\partial^2 U^*}{\partial Y^2}\right)-\varepsilon^2.\frac{1}{\nu_{nf}\alpha_f}.\frac{U^*}{Da}+\varepsilon^2\frac{\beta_{nf}}{\beta_f}\ \ Ra.Pr.\theta\ sin\gamma \tag{10}$$

$$U^*\frac{\partial V^*}{\partial X}+V^*\frac{\partial V^*}{\partial Y}=-\varepsilon^2\frac{\partial P}{\partial Y}+\varepsilon.\frac{1}{\nu_{nf}\alpha_f}.\left(\frac{\partial^2 V^*}{\partial X^2}+\frac{\partial^2 V^*}{\partial Y^2}\right)-\varepsilon^2.\frac{1}{\nu_{nf}\alpha_f}.\frac{V^*}{Da}+\varepsilon^2\frac{\beta_{nf}}{\beta_f}\ \ Ra.Pr.\theta\ cos\gamma \tag{11}$$

$$U^*\frac{\partial \theta}{\partial X}+V^*\frac{\partial \theta}{\partial Y}=\frac{\alpha_{eff}}{\alpha_f}\left(\frac{\partial^2 \theta}{\partial X^2}+\frac{\partial^2 \theta}{\partial Y^2}\right)+\lambda\theta \tag{12}$$

The following describes the dimensionless variables in Equations 9 - 12.

$$X=\frac{x}{L};Y=\frac{y}{L};U^*=\frac{u^*.L}{\alpha_f};V^*=\frac{v^*.L}{\alpha_f};P=\frac{p.L^2}{\rho_{nf}\alpha_f^2};\theta=\frac{T-T_c}{T_h-T_c};Ra=\frac{g\beta(T-T_c)L^3}{\nu_f\ \alpha_f};Pr=\frac{\nu_f}{\alpha_f};Da=\frac{K}{L^2}\ ;\ \lambda=\frac{Q_\circ.L^2}{\alpha_f};\ \Delta T=\frac{q^{"}L}{k_f} \tag{13}$$

While the thermophysical properties are defined as [66]:

$$\begin{aligned}\rho_{nf}&=(1-\phi)\rho_f+\phi\rho_{sp}\\(\rho c_p)_{nf}&=(1-\phi)\left(\rho c_p\right)_f+\phi(\rho c_p)_{sp}\\(\rho\beta)_{nf}&=(1-\varphi)(\rho\beta)_f+\varphi(\rho\beta)_{sp}\\\alpha_{eff}&=\frac{k_{eff}}{\left(\rho.C_p\right)_{nf}}\end{aligned} \tag{14}$$

$$\alpha_{nf} = \frac{k_{nf}}{(\rho . C_p)_{nf}}$$

$$k_{eff} = (1-\varepsilon)k_{sp} + \varepsilon k_{nf}$$

$$\mu_{nf} = \frac{\mu_f}{(1-\phi)^{2.5}}$$

$$k_{nf} = \frac{(k_{sp}+2k_{sp}) - 2\phi(k_f - k_{sp})}{(k_f+2k_{sp}) + \phi(k_f + k_{sp})} k_f$$

The local Nu number of the hot sinusoidal-corrugated vertical walls using a dimensionless temperature is expressed as :

$$Nu_{Lo} = -\frac{k_{eff}}{k_f}\left(\frac{\partial \theta_s}{\partial n}\right)_w \tag{15}$$

The terms $(\partial\theta_s/\partial n)_w$ is the normal temperature gradient to the hot sinusoidal-corrugated walls for the solid phase, respectively. The local Nu number is integrated along the hot wall surface yields the average Nussult number around the left lower and upper sinusoidal walls [38,53].

$$Nu_{av} = \frac{1}{B}\int_M^B Nu_{Lo}\, dn \tag{16}$$

*B*= 1-*L/2* and *M* = 0 For the left lower vertical wall

*B*= 1- *L/2* and *M* = *L/2* For the left upper sinusoidal wall

The stream function is used to describe fluid motion and is formed from the velocity components $U^*$ and $V^*$. For 2-dimensional flow, the following are the relations between the components of velocity and stream function [66]:

$$U^* = \frac{\partial \psi}{\partial Y}, \qquad V^* = -\frac{\partial \psi}{\partial X} \tag{17}$$

$$\frac{\partial^2 \psi}{\partial X^2} + \frac{\partial^2 \psi}{\partial Y^2} = \frac{\partial U^*}{\partial Y} - \frac{\partial V^*}{\partial X} \tag{18}$$

## 4. Entropy Generation and Bejan Number

The local entropy production rate is calculated by adding the entropy produced by the two sources of heat flow and fluid friction [12]:

$$s_{gen} = \dot{s}_{gen,HF} + \dot{s}_{gen,FF} \tag{19}$$

$$\dot{s}_{gen,HF} = \frac{k_{nf}}{T_0^2}\left[\left(\frac{\partial T}{\partial x}\right)^2 + \left(\frac{\partial T}{\partial y}\right)^2\right] \tag{20}$$

$$\dot{s}_{gen,FF} = \frac{\mu_{nf}}{KT_0}\left[(u^{*2} + v^{*2}) + K\left\{2\left[\left(\frac{\partial u^*}{\partial x}\right)^2 + \left(\frac{\partial v}{\partial y}\right)^2\right] + (\frac{\partial u^*}{\partial y} + \frac{\partial v^*}{\partial x})^2\right\}\right] \tag{21}$$

Local Sgen may be expressed in dimensionless shape [13]:

$$S_{gen} = \frac{k_{eff}}{k_f}\left[\left(\frac{\partial\theta}{\partial X}\right)^2 + \left(\frac{\partial\theta}{\partial Y}\right)^2\right] + \Gamma\left[(U^{*2} + V^{*2}) + Da\left\{2\left[\left(\frac{\partial U^*}{\partial X}\right)^2 + \left(\frac{\partial V^*}{\partial Y}\right)^2\right] + (\frac{\partial U^*}{\partial Y} + \frac{\partial V^*}{\partial X})^2\right\}\right] \quad (22)$$

The value of Γ in the above equation is taken as 0.01, and the local Sgen in dimensionless form becomes:

$$S_{gen} = s_{gen}.\frac{L_c^2}{k_f}\left(\frac{T_0}{\Delta T}\right)^2 \quad (23)$$

Total Sgen in a dimensionless form is generated by integrating local Sgen across all computing domains as follows:

$$\dot{S}_{gen,T} = \int S_{gen}.dA \quad (24)$$

The Bejan number illustrates the strength of irreversibility induced by Q and Sgen as [38]:

$$Be_T = \frac{\dot{S}_{gen,HF}}{\dot{S}_{gen,T}} \quad (25)$$

As $Be_T$ approaches 1, the irreversibility of H.T. becomes dominating. The irreversibility of the viscous effect dominates the processes when $Be_T$ is significantly lower than 1/2. The H.T. and viscous effects produce equal Sgen when $Be_T$ = 1/2.

The following boundary conditions develop in the dimensionless forms:

$U = 0\,;\ V = 0\ ;\quad \theta = 1\,, \psi = 0$ at the hot left walls of the enclosure (26)

$U = 0\,;\ V = 0\ ;\quad \theta = 0, \psi = 0$ at the cold right walls of the enclosure (27)

$U = 0\,;\ V = 0\ ;\quad \frac{\partial\theta}{\partial Y} = 0\,, \psi = 0$ at the insulated walls (28)

## 5. Numerical Procedure

The Galerkin FEM ( GFEM) is employed to solve the Equations (9-12) with the boundary conditions (26-28). Each flow variable within the computational domain is represented by a different order of Triangular Lagrange finite elements. The governing equations are formulated toward the weak (or weighted-integral) formulation. The GFEM was employed to solve the energy and momentum equations, yielding the following results:

$$\int_{\Omega}\left(\Phi_{\mathrm{i}}.\mathrm{U}^{*\mathrm{k}}.\frac{\partial \mathrm{U}^{*\mathrm{k}}}{\partial \mathrm{X}}+\Phi_{\mathrm{i}}.\mathrm{V}^{*\mathrm{k}}.\frac{\partial \mathrm{U}^{*\mathrm{k}}}{\partial \mathrm{Y}}\right)dX.dY=-\varepsilon^{2}\int_{\Omega}\frac{\partial \Phi_{\mathrm{i}}}{\partial \mathrm{X}}\left(\frac{\partial \mathrm{U}^{*\mathrm{k}}}{\partial \mathrm{X}}+\frac{\partial \mathrm{V}^{*\mathrm{k}}}{\partial \mathrm{Y}}\right)dX.dY$$
$$+\varepsilon.\frac{\nu_{nf}}{\alpha_{f}}.\int_{\Omega}\Phi_{\mathrm{i}}\left(\frac{\partial^{2}\mathrm{U}^{*\mathrm{k}}}{\partial \mathrm{X}^{2}}+\frac{\partial^{2}\mathrm{U}^{*\mathrm{k}}}{\partial \mathrm{Y}^{2}}\right)-\frac{\varepsilon^{2}}{Da}.\frac{\nu_{nf}}{\alpha_{f}}\int_{\Omega}\Phi_{\mathrm{i}}U^{*k}\,dX.dY \tag{29}$$
$$+\varepsilon^{2}\frac{(\rho\beta)_{nf}}{\rho_{nf}\,\beta_{f}}\;Ra.Pr.sin\gamma\int_{\Omega}\Phi_{\mathrm{i}}\theta^{k}\,dX.dY$$

$$\int_{\Omega}\left(\Phi_{\mathrm{i}}.\mathrm{U}^{*\mathrm{k}}.\frac{\partial \mathrm{V}^{*\mathrm{k}}}{\partial \mathrm{X}}+\Phi_{\mathrm{i}}.\mathrm{V}^{*\mathrm{k}}.\frac{\partial \mathrm{V}^{*\mathrm{k}}}{\partial \mathrm{Y}}\right)dX.dY=-\varepsilon^{2}\int_{\Omega}\frac{\partial \Phi_{\mathrm{i}}}{\partial \mathrm{Y}}\left(\frac{\partial \mathrm{U}^{*\mathrm{k}}}{\partial \mathrm{X}}+\frac{\partial \mathrm{V}^{*\mathrm{k}}}{\partial \mathrm{Y}}\right)dX.dY$$
$$+\varepsilon.\frac{\nu_{nf}}{\alpha_{f}}.\int_{\Omega}\Phi_{\mathrm{i}}\left(\frac{\partial^{2}\mathrm{V}^{*\mathrm{k}}}{\partial \mathrm{X}^{2}}+\frac{\partial^{2}\mathrm{V}^{*\mathrm{k}}}{\partial \mathrm{Y}^{2}}\right)dX.dY-\frac{\varepsilon^{2}}{Da}.\frac{\nu_{nf}}{\alpha_{f}}\int_{\Omega}\Phi_{\mathrm{i}}V^{*k}\,dX.dY \tag{30}$$
$$+\;\varepsilon^{2}\frac{(\rho\beta)_{nf}}{\rho_{nf}\,\beta_{f}}\;Ra.Pr.cos\gamma\int_{\Omega}\Phi_{\mathrm{i}}\theta^{k}\,dX.dY$$

$$\int_{\Omega}\left(\Phi_{\mathrm{i}}.\mathrm{U}^{*\mathrm{k}}.\frac{\partial \theta^{\mathrm{k}}}{\partial \mathrm{X}}+\Phi_{\mathrm{i}}.\mathrm{V}^{*\mathrm{k}}.\frac{\partial \theta^{\mathrm{k}}}{\partial \mathrm{Y}}\right)dX.dY=\frac{\alpha_{eff}}{\alpha_{f}}\int_{\Omega}\Phi_{\mathrm{i}}\left(\frac{\partial^{2}\theta^{\mathrm{k}}}{\partial \mathrm{X}^{2}}+\frac{\partial^{2}\theta^{\mathrm{k}}}{\partial \mathrm{Y}^{2}}\right)+\lambda\int_{\Omega}\Phi_{\mathrm{i}}\theta^{k}\,dX.dY \tag{31}$$

Next, the variables' ranges are then subjected to the following base extensions:

$$U^{*}=\sum_{j=1}^{N}U_{J}^{*}\,\Phi_{\mathrm{i}}(X,Y),\quad V^{*}=\sum_{j=1}^{N}V_{J}^{*}\,\Phi_{\mathrm{i}}(X,Y),\quad P=\sum_{j=1}^{N}P_{J}^{*}\,\Phi_{\mathrm{i}}(X,Y),$$
$$\theta=\sum_{j=1}^{N}\theta_{J}^{*}\,\Phi_{\mathrm{i}}(X,Y) \tag{32}$$

However, the residual pattern of equations is derived by integrating the weak appearance of equations across the discrete region:

$$R(1)_{i}=\sum_{j=1}^{M}U_{j}^{*}\int_{\Omega}\left[\left(\sum_{j=1}^{M}\mathrm{U}_{\mathrm{j}}^{*}\,\Phi_{\mathrm{j}}\right).\frac{\partial \Phi_{\mathrm{j}}}{\partial \mathrm{X}}+\left(\sum_{j=1}^{M}\mathrm{V}_{\mathrm{j}}^{*}\,\Phi_{\mathrm{j}}\right).\frac{\partial \Phi_{\mathrm{j}}}{\partial \mathrm{Y}}\right]\Phi_{\mathrm{i}}dX.dY$$
$$+\varepsilon^{2}\left[\sum_{j=1}^{M}U_{j}^{*}\int_{\Omega}\frac{\partial \Phi_{\mathrm{i}}}{\partial \mathrm{X}}\frac{\partial \Phi_{\mathrm{j}}}{\partial \mathrm{X}}dX.dY+\sum_{j=1}^{M}V_{j}^{*}\int_{\Omega}\frac{\partial \Phi_{\mathrm{i}}}{\partial \mathrm{X}}\frac{\partial \Phi_{\mathrm{j}}}{\partial \mathrm{Y}}dX.dY\right]$$
$$+\varepsilon.\frac{\nu_{nf}}{\alpha_{f}}.\sum_{j=1}^{M}U_{j}^{*}\int_{\Omega}\left[\frac{\partial \Phi_{\mathrm{i}}}{\partial \mathrm{X}}.\frac{\partial \Phi_{\mathrm{j}}}{\partial \mathrm{X}}+\frac{\partial \Phi_{\mathrm{i}}}{\partial \mathrm{Y}}.\frac{\partial \Phi_{\mathrm{j}}}{\partial \mathrm{Y}}\right]\mathrm{dXdY}+\frac{\varepsilon^{2}}{Da}.\frac{\nu_{nf}}{\alpha_{f}}\int_{\Omega}\left(\sum_{j=1}^{M}\mathrm{U}_{\mathrm{j}}^{*}\,\Phi_{\mathrm{j}}\right)\Phi_{\mathrm{i}}\,dX.dY \tag{33}$$
$$+\varepsilon^{2}\frac{(\rho\beta)_{nf}}{\rho_{nf}\,\beta_{f}}\;Ra.Pr.sin\gamma\int_{\Omega}\left(\sum_{j=1}^{M}\theta_{\mathrm{j}}\,\Phi_{\mathrm{j}}\right)\Phi_{\mathrm{i}}\,dX.dY$$

$$R(2)_i = \sum_{j=1}^{M} V_j^* \int_\Omega \left[ \left( \sum_{j=1}^{M} \mathrm{U_j^*}\, \Phi_\mathrm{j} \right) . \frac{\partial \Phi_\mathrm{j}}{\partial \mathrm{X}} + \left( \sum_{j=1}^{M} \mathrm{V_j^*}\, \Phi_\mathrm{j} \right) . \frac{\partial \Phi_\mathrm{j}}{\partial \mathrm{Y}} \right] \Phi_\mathrm{i} dX.dY$$
$$+ \varepsilon^2 \left[ \sum_{j=1}^{M} U_j^* \int_\Omega \frac{\partial \Phi_\mathrm{i}}{\partial \mathrm{X}} \frac{\partial \Phi_\mathrm{j}}{\partial \mathrm{X}} dX.dY + \sum_{j=1}^{M} V_j^* \int_\Omega \frac{\partial \Phi_\mathrm{i}}{\partial \mathrm{X}} \frac{\partial \Phi_\mathrm{j}}{\partial \mathrm{Y}} dX.dY \right]$$
$$+ \varepsilon . \frac{\nu_{nf}}{\alpha_f} . \sum_{j=1}^{M} V_j^* \int_\Omega \left[ \frac{\partial \Phi_\mathrm{i}}{\partial \mathrm{X}} . \frac{\partial \Phi_\mathrm{j}}{\partial \mathrm{X}} + \frac{\partial \Phi_\mathrm{i}}{\partial \mathrm{Y}} . \frac{\partial \Phi_\mathrm{j}}{\partial \mathrm{Y}} \right] \mathrm{dXdY} + \frac{\varepsilon^2}{Da} . \frac{\nu_{nf}}{\alpha_f} \int_\Omega \left( \sum_{j=1}^{M} \mathrm{V_j^*}\, \Phi_\mathrm{j} \right) \Phi_\mathrm{i}\, dX.dY \quad (34)$$
$$+ \varepsilon^2 \frac{(\rho\beta)_{nf}}{\rho_{nf}\, \beta_f}\ Ra.Pr.cos\gamma \int_\Omega \left( \sum_{j=1}^{M} \theta_\mathrm{j}\, \Phi_\mathrm{j} \right) \Phi_\mathrm{i}\, dX.dY$$

$$R(3)_i = \sum_{j=1}^{M} \theta_j \int_\Omega \left[ \left( \sum_{j=1}^{M} \mathrm{U_j^*}\, \Phi_\mathrm{j} \right) . \frac{\partial \Phi_\mathrm{j}}{\partial \mathrm{X}} + \left( \sum_{j=1}^{M} \mathrm{V_j^*}\, \Phi_\mathrm{j} \right) . \frac{\partial \Phi_\mathrm{j}}{\partial \mathrm{Y}} \right] \Phi_\mathrm{i} dX.dY + \varepsilon . \sum_{j=1}^{M} \theta_j \int_\Omega \left[ \frac{\partial \Phi_\mathrm{i}}{\partial \mathrm{X}} . \frac{\partial \Phi_\mathrm{j}}{\partial \mathrm{X}} + \frac{\partial \Phi_\mathrm{i}}{\partial \mathrm{Y}} . \frac{\partial \Phi_\mathrm{j}}{\partial \mathrm{Y}} \right] \mathrm{dXdY}$$
$$+ \lambda \int_\Omega \left( \sum_{j=1}^{M} \theta_j\, \Phi_\mathrm{j} \right) \Phi_\mathrm{i}\, dX.dY \quad (35)$$

Where The superscript k represents the relative index, whereas the subscripts I and j represent the residual and node number, respectively. The number of iterations is determined by M. Integrals are also produced using second-order Gaussian quadrature. The Newton-Raphson iteration approach is used to iteratively calculate the residual equations using the following closure form of all field variables:

$$\chi = \frac{\sum_{i,j} \left| \Gamma_{\mathrm{i,j}}^{\mathrm{t+1}} - \Gamma_{\mathrm{i,j}}^{\mathrm{t}} \right|}{\left| \Gamma_{\mathrm{i,j}}^{\mathrm{t+1}} \right|} \leq 10^{-6} \quad (36)$$

Where $\chi$ denotes the tolerance; Γ and t are any of the computed field variables and the iteration number, respectively.

## 6. Results and Discussion

In this work, the triangular mesh distribution is presented in Fig. 2. The grid sensitivity assessments are carried out to find the grid-independence solutions for the field variables, as indicated in Table 2. The mean Nusselt number is chosen to predict the mesh independence since it is a global parameter that does not change while the solution is stable. In the same table, five meshes were tested with an average Nu on the surface for Da = $10^{-3}$, Ra = $10^5$, $\phi$ = 0.02, λ = 10, A

= 0.04 L, and n = L/6. After 22024 elements with a finer grid, the average Nusselt number changes insignificantly. The sensitivity is established to be exceptional, confirming the current computational analysis. Based on the results presented in Table 2, a comparative finer mesh with 26548 elements has been selected to solve the whole equations of the current study.

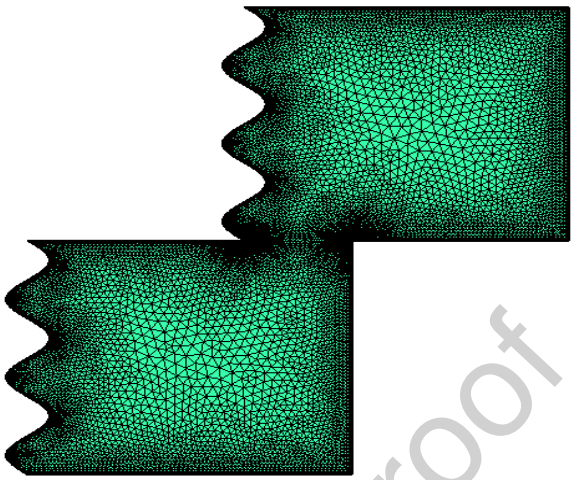

**Fig. 2** Un-Structural mesh distribution of the present study

**Table 2** Grid independent test average Nusselt number on the surface at (Da = $10^3$, Ra = $10^5$, φ = 0.02, λ = 10, A = 0.04 L, and n = L/6)

| Grid | Domain elements | Boundary elements | Time (Sec) | $Nu_{avh}$ | $\|Error\|$ (%) | $Nu_{avl}$ | Error (%) | $\|\psi_{min}\|$ | Error (%) |
|---|---|---|---|---|---|---|---|---|---|
| G1 | 4165 | 289 | 16 | 2.4801 | - | 1.7230 | - | 1.7304 | - |
| G2 | 6206 | 356 | 20 | 2.4925 | 0.49 | 1.7228 | 0.012 | 1.7367 | 0.36 |
| G3 | 10069 | 489 | 24 | 2.5495 | 2.23 | 1.7306 | 0.45 | 1.7389 | 0.126 |
| G4 | 22024 | 792 | 42 | 2.5842 | 1.34 | 1.7335 | 0.167 | 1.7417 | 0.16 |
| G5 | 26548 | 792 | 50 | 2.5830 | 0.046 | 1.7338 | 0.017 | 1.7421 | 0.022 |

The computer code was validated using the same problem that Al-Zamily [12] studied for a square enclosure comprising multi-layers, porous medium, and nanofluid with varying values of Ra and volume fraction ($\phi$), as shown in Table 3. Fig. 3 depicts the initial validation for the isotherm and streamline contours. Fig. 4 displays the second validation study, which compares the contours of the stream function for case-1 at Ra = $10^5$, Da = $10^{-3}$, λ = 0, and $L_{bm}$ = L/5. Furthermore, the current computational numerical analysis is validated against the previous study published by Al-Zamily [12] with Sgen owing to friction flow and heat flow within the enclosure with Ra = $10^4$, Da = $10^{-3}$, Φ = 0, and λ = 0 as shown in Fig. 4. The findings of the two studies show a significant level of agreement. These comparisons provided a high confidence level in the proposed computational

investigation to address the physical problem. Fig. 5 compared the effects of Sgen for a porous cavity when Ra = $10^4$, Da = $10^{-3}$, Φ = 0, λ = 0 with the results of Ali Meerali Jasim Al-Zamily [12]. As observed, the domain of Sgen in all three domains is identical to that of a previous study, confirming the accuracy of the present numerical approach in predicting Sgen. Furthermore, the results of the average Nu for this case of study at different Ra and Φ numbers are presented in Table 3, which also approves the results of the current study.

**Table 3** Comparison of the average Nusselt number along the hot wall

| **Da = 0.1** | **Al-Zamily** [12] | | | **Present study** | | | **Error (%)** | | |
|---|---|---|---|---|---|---|---|---|---|
| Ra | $\varphi = 0$ | $\varphi = 0.05$ | $\varphi = 0.1$ | $\varphi = 0$ | $\varphi = 0.05$ | $\varphi = 0.1$ | $\varphi = 0$ | $\varphi = 0.05$ | $\varphi = 0.1$ |
| $10^4$ | 2.2 | 2.27 | 2.34 | 2.1939 | 2.2603 | 2.3465 | -0.27 | -0.429 | 0.277 |
| $10^5$ | 4 | 4.05 | 4.1 | 3.9619 | 3.9910 | 4.0025 | -0.96 | -1.147 | -2.43 |
| $10^6$ | 7.1 | 7.25 | 7.4 | 7.1316 | 7.2513 | 7.3284 | 0.44 | 0.0179 | -0.97 |
| $10^7$ | 11.9 | 13.001 | 13.2 | 12.075 | 12.654 | 12.810 | 1.449 | -2.742 | 3.04 |

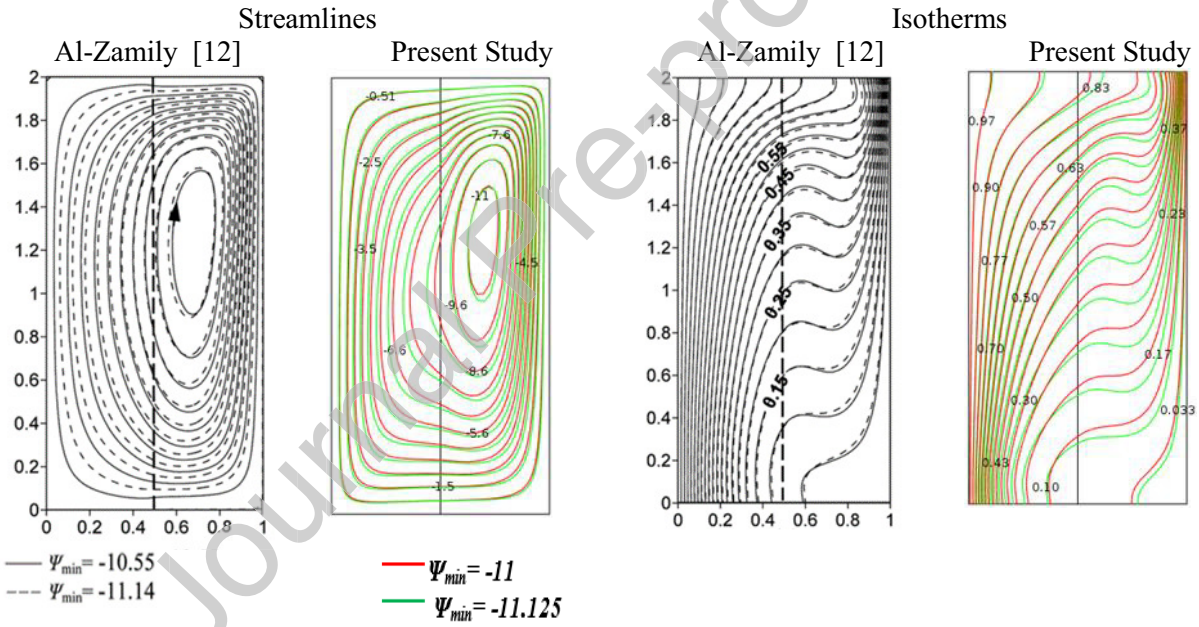


**Fig. 3** Comparison of streamlines and isotherms between Al-Zamily work [12] and the present study

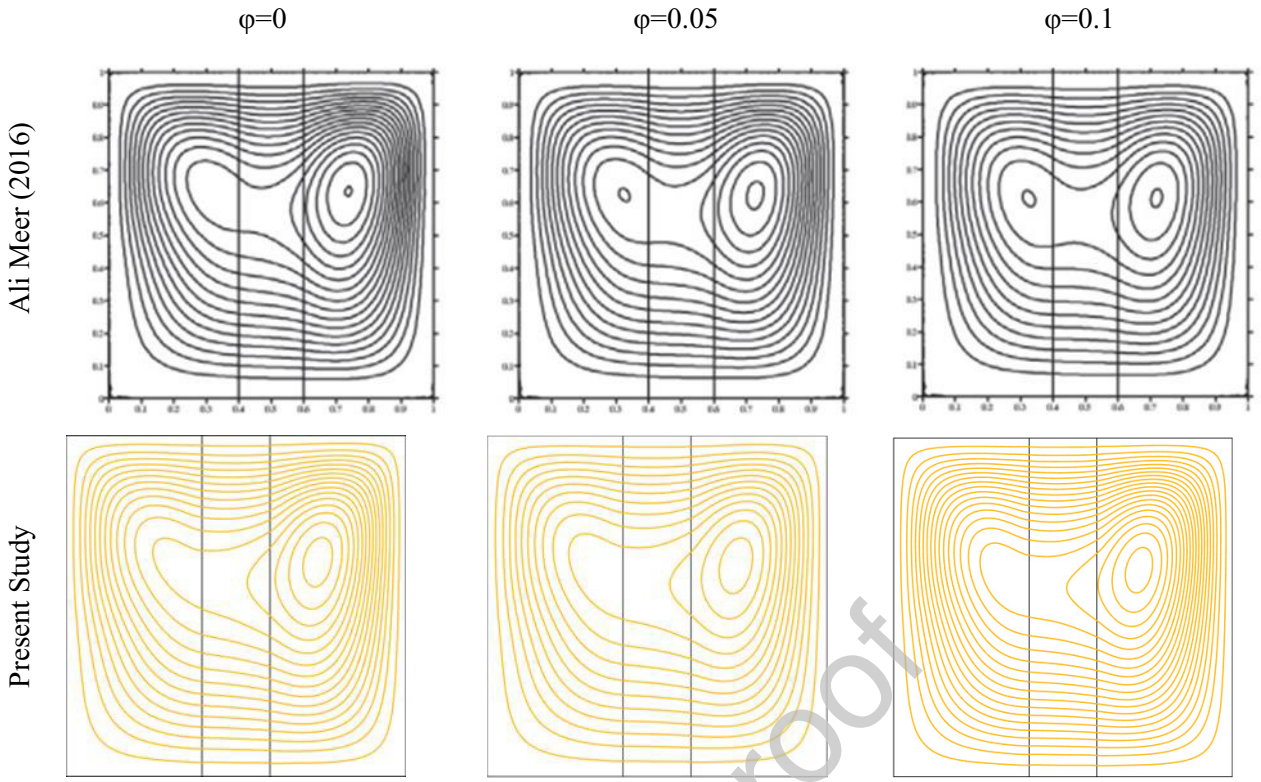


**Fig. 4** Stream function comparison for a different volume fraction between Al-Zamily [12] and the present study of case-1, Ra = $10^5$, Da = $10^{-3}$, λ = 0, and $L_{bm}$ = L/5

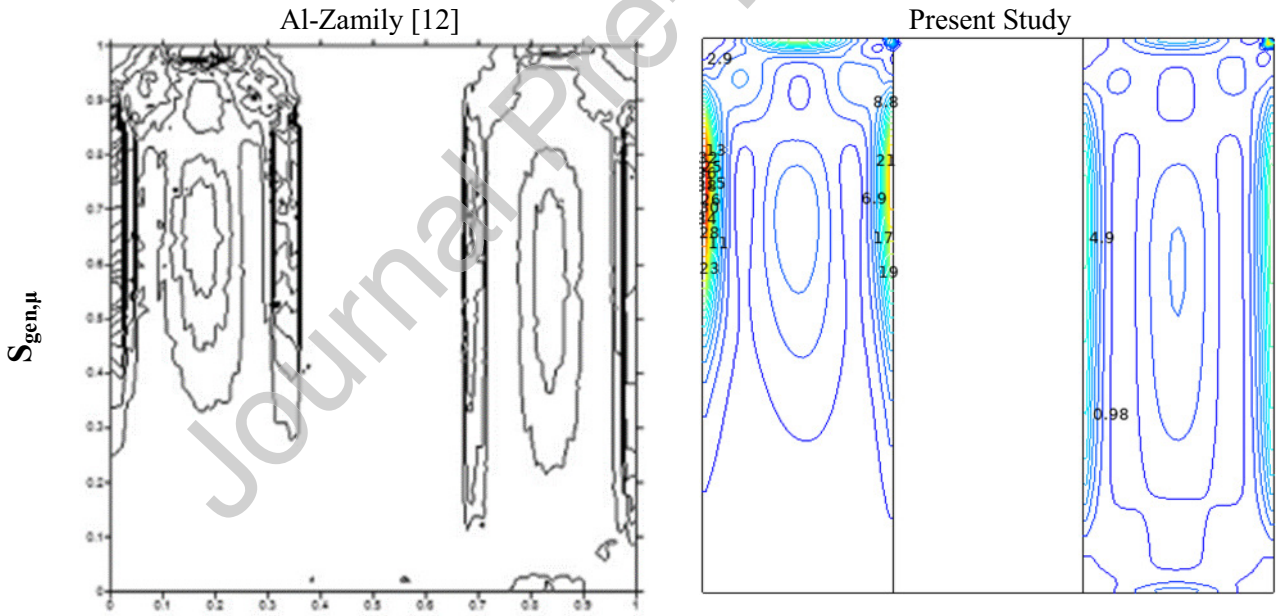

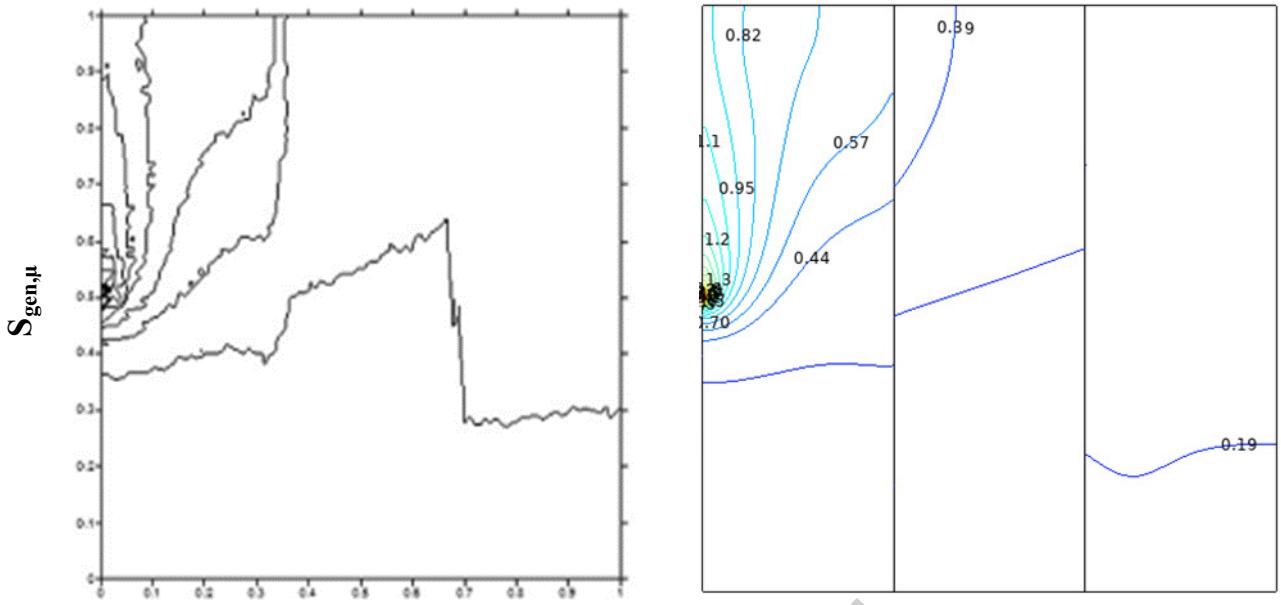


**Fig. 5** Entropy generation due to friction ($S_{gen,\mu}$) and total entropy generation ($S_{gen,T}$) comparison between Al-Zamily [12] and the present study Ra = $10^4$, Da = $10^{-3}$, φ= 0, and λ = 0

Fig. 6 depicts the streamlines for staggered enclosure when the tilt angle is zero at different Ra and Da numbers. As observed, increasing the Ra number increased the intensity of streamlines as well as their maximum values. Furthermore, increasing the Da improves the absolute values of streamlines in maximum and minimum values in most cases. The physical reason is increasing the N.C. current intensity with increasing Ra and Da. Fig. 7 demonstrates the isotherm lines for the cases presented in Fig. 6. It can be observed that higher Ra numbers provide a more N.C. effect, shifting higher temperatures from the left-side wavy to the right-side flat walls. Furthermore, temperatures are raised from the bottom to the top walls. Additionally, higher Da numbers resulted in increased H.T. from the left to the right side, and higher temperatures towards the top wall of the staggered enclosure. This is due to the domination of the N.C. mode with increasing the Ra and Da, which in turn change the isotherms lines shape from the vertical shape at low Ra and Da (conduction mode) into more horizontal shape lines (N.C. mode). Fig. 8 provides information about the entropy generation and Bejan number at different Rayleigh numbers and Darcy numbers in each of the preceding situations. The figure illustrates the influence of high Rayleigh numbers on entropy generation, showing that as the Rayleigh number increases, convection becomes the dominant